Applied Thermal Engineering 279 (2025) 127702

Contents lists available at ScienceDirect

Applied Thermal Engineering

journal homepage: www.elsevier.com/locate/apthermeng

Research Paper

Coupled heat transfer mechanism in microencapsulated phase change material: thermal radiation, convection, and phase change

Si Yang [a], Hangbin Zhao [b,*], Renwei Tang [b], Xiaobin Tang [a,c,**]

[a] Department of Nuclear Science and Technology, Nanjing University of Aeronautics and Astronautics, Nanjing 211106, China
[b] College of Astronautics, Nanjing University of Aeronautics and Astronautics, Nanjing 211106, China
[c] Key Laboratory of Advanced Nuclear Technology and Radiation Protection, Ministry of Industry and Information Technology, Nanjing 211106, China

ARTICLE INFO

Keywords:
Microencapsulated phase-change material
Thermal radiation
Mie scatter
Heat convection
Phase change

ABSTRACT

The reactor cavity cooling system (RCCS) plays a crucial role in ensuring the safety of the high-temperature gas-cooled reactor (HTGR). However, the existing designs struggle to meet the heat dissipation demands of higher-power HTGR. Microencapsulated phase-change material (MPCM) slurry offers significant advantages, including high heat capacity and excellent stability. Hence, this study proposes its potential to optimize the cooling efficacy of the RCCS. To achieve this, a comprehensive understanding of the coupled heat transfer mechanisms of MPCM is essential. In this study, a computational program is developed to simulate these coupled heat transfer processes. The reliability of this program is validated by comparing its results with the computational results of commercial software. Additionally, the program enables accurate transient heat transfer calculations for MPCM. Based on the program, the effects of light intensity, core–shell ratio, and MPCM diameter on the heat transfer process and phase-change process are systematically analyzed. A key insight of this study is the identification of two distinct diameter classifications for MPCM: the critical diameter and the most effective diameter. These classifications emerged from observed patterns in how MPCM diameter influences heat transfer performance. Based on these findings, empirical correlation formulas relating the two diameters and light intensity are developed. These discoveries may provide valuable guidance for selecting the optimal particle size for the application of MPCM in RCCS and other MPCM-integrated system.

1. Introduction

The reactor cavity cooling cystem (RCCS) is a critical safety component in high-temperature gas-cooled reactor (HTGR) [1]. Its primary function is to passively remove heat from the reactor compartment under all operating conditions, including normal operation, where it cools and protects the reactor structure, and accident scenarios, where it transfers decay heat to the ultimate heat sink [2]. Among the various RCCSs, the most critical component is the structure responsible for radiative-convective coupled heat transfer with the reactor cavity. Fig. 1 illustrates the radiative-convective heat transfer design configurations employed in three HTGR types: the HTR-PM, HTTR, and HTGR-350 [3].

In these reactors, excess heat from the reactor must first be transferred to the RCCS via radiative heat transfer from the reactor cavity wall and convective heat transfer through air. The heat is then conducted from the outer wall (tube or pool) to the inner wall (tube or pool). Subsequently, the inner wall transfers the heat to the cooling medium via convective heat transfer, and the cooling medium ultimately removes the heat through fluid flow. However, this multistep heat transfer process introduces inefficiencies, complicating the effective transfer of heat to the cooling medium. Furthermore, the use of the limited natural circulation capacity of the water or limited specific heat capacity of the air as the cooling medium, poses challenges for rapid heat removal from the reactor compartment. To address the cooling requirements of HTGR with higher power output [4], further optimization of the RCCS's cooling efficiency is essential.

Heat transfer can be improved through two major approaches: optimizing the heat transfer structure [5] and enhancing the thermal properties of the working medium [6]. Enhancing the working medium can enable efficient heat dissipation, reduction in energy consumption, and improvement in the overall performance of thermal systems [7]. Microencapsulated phase-change material (MPCM) slurry offers significant advantages, including high energy storage density and efficient

* Corresponding author at: College of Astronautics, Nanjing University of Aeronautics and Astronautics, Room B427, Nanjing 211106, China.
** Corresponding author at: College of Materials Science and Technology, Nanjing University of Aeronautics and Astronautics, Room 224, Nanjing 211106, China.
E-mail addresses: zhaohangbin@nuaa.edu.cn (H. Zhao), tangxiaobin@nuaa.edu.cn (X. Tang).

https://doi.org/10.1016/j.applthermaleng.2025.127702
Received 29 March 2025; Received in revised form 19 July 2025; Accepted 29 July 2025
Available online 30 July 2025

Nomenclature

$\overline{\rho}$	Average density of the MPCM [kg·m^{-3}]	*Pe*	Peclet number
$\overline{c_p}$	Average heat capacity of MPCM [J·kg^{-1}·K^{-1}]	*Pr*	Prandtl number
τ	Time [s]	Q_{abs}	Absorption efficiency
χ	Size parameter	Q_e	Extinction efficiency
λ	Wavelength [m]	Q_s	Scattering efficiency
G	Projection area of the MPCM [m·s^{-2}]	R	Radius of the MPCM [m]
h	Convective heat transfer coefficient [W·K^{-1}·m^{-2}]	*Re*	Reynolds number
I	Light intensity [W·m^{-2}]	*T*	Temperature [K]
k	Thermal conductivity [W·m^{-1}·K^{-1}]	T_L	Temperature of the base fluid [K]
Nu	Nusselt number	T_m	Melt point of the phase change material [K]
		V_c	Core volume of the MPCM [m^3]

thermal regulation. Moreover, they can maintain almost constant temperatures during phase transitions [8], rendering them ideal for applications in thermal energy storage, heating, ventilation and air conditioning systems [9].

MPCM is an advanced structure designed to store and release thermal energy during phase transitions. It comprises a core material, which is a phase-change material (PCM), encapsulated within a protective shell. The shell is typically made of polymers or other materials that prevent leakage, improve stability, and enhance the management of the PCM [7]. Numerous studies have investigated the flow and heat transfer characteristics of MPCM slurry. Zeng [8] investigated the convective heat transfer characteristics of an MPCM slurry flowing in a circular tube. Experimental and numerical results showed that the average Nusselt number was mainly influenced by the *Ste* number. Sabbah et al. [10] showed that the local heat transfer coefficient of MPCM slurry is highly dependent on the location of the phase-change interface. Lenert et al. [11] showed that the local maximum Nusselt number increases with higher MPCM mass fractions and greater latent heat but decreases with a wider melting range and higher heat flux. To address the issue of insufficient accuracy resulting from the empirical modification in previous studies, Lin et al. [12] developed a new multiscale model to simulate the flow and heat transfer of MPCM slurry within a circular tube. In this model, the liquid volume fraction of the PCM was calculated, and the numerical results were consistent with experimental data. Zhao et al. [13] used two-phase Eulerian and multiscale coupling models to simulate the heat transfer process of MPCM slurry in a space radiator. They found that the heat dissipation capacity of a sample with the MPCM could be increased by 5 % compared with that of a sample with pure water.

Hence, this paper proposes a novel RCCS design to overcome the aforementioned limitations by using MPCM. Unlike the HTR-PM, the new design replaces the water tube wall adjacent to the pressure vessel with glass exhibiting high thermal radiation transparency and substitutes the cooling medium with MPCM slurry. In this configuration, excess reactor heat is primarily transferred via thermal radiation, penetrates the glass tube wall, and is directly absorbed by the MPCM slurry. This modification significantly simplifies the heat transfer process by eliminating intermediate steps. Furthermore, the integration of MPCM enhances the cooling medium's heat-carrying capacity, improving overall thermal management.

However, the heat transfer mechanism of MPCM has become notably complex, encompassing thermal radiation, convection, and phase change, as shown in Fig. 2. These three heat transfer processes are intricately coupled. Thermal radiation serves as the primary heat source and is converted into thermal energy via photothermal conversion. The conversion efficiency is influence by the temperature-dependent optical properties of the material, particle size, and phase-change process. The phase-change process is influenced by thermal radiation and convective heat transfer. Convection is influence by the temperature-dependent thermal properties and particle size of the material.

Previous studies have investigated the overall heat transfer performance of MPCM slurry in applications such as solar water heaters [14], photovoltaic panels [15], and direct-absorption solar collectors [16], which share a similar heat transfer environment with the newly proposed RCCS design. Ma et al. [16] used MPCM slurry in a direct-absorption solar collector to enhance the efficiency of the solar collector. Numerical results showed that the incorporation of the microcapsules increased the amount of heat absorbed, reduced the surface temperature, and ultimately improved the overall system efficiency. However, the simulation assumed constant optical properties for the MPCM and did not consider the phase-change process of the internal core material. Ran et al. [17] developed a model of a flat-plate solar collector incorporating MPCM slurry. Simulation results showed that the thermal efficiency of the solar collector model increased with higher mass fractions and greater latent heat of the MPCM slurry but decreased with increasing solar radiation intensity. In the simulation, the phase-

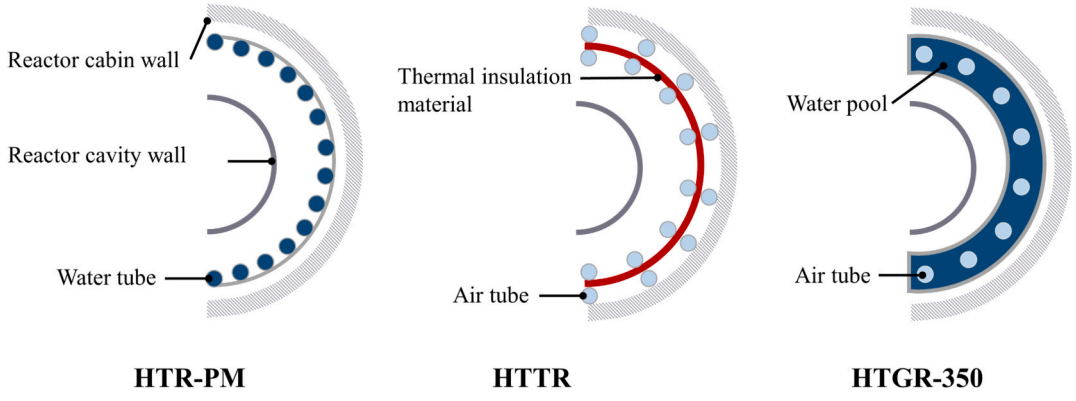

Fig. 1. RCCS of the HTR-PM, HTTR, and HTGR-350.

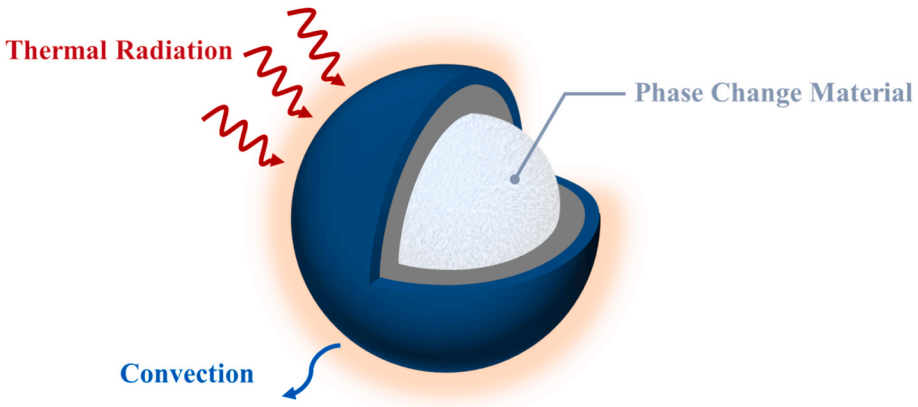

Fig. 2. Heat transfer mechanism of MPCM.

change process was simplified to a change in heat capacity, while other thermophysical parameters remained constant. Kharazmi et al. [18] investigated the thermal performance of direct absorption solar-evacuated tube collectors using various working fluids, including CuO, CuO/Al_2O_3 binary, and CuO nanofluids combined with MPCMs. Results showed that combining MPCMs with a CuO nanofluid enhanced collector efficiency by 4.53 % and reduced heat loss by 5.84 %. To further improve photothermal conversion efficiency, Wang et al. [19] investigated the impact of MPCM and multiwalled carbon nanotubes dispersed in water and ethanol as base fluids on the performance of direct absorption solar collectors. Although the reflectance of water, ethanol, and carbon nanotubes remained very low, the transmittance significantly increased with the incorporation of MPCM. Huang et al. [20] proposed a novel design for MPCM incorporated with black phosphorus sheets. Experimental results show that the solar energy storage efficiency of the novel design was three times that of the original design without the sheets.

Several studies have investigated direct solar absorption devices using MPCM. Nevertheless, only a few have analyzed the coupling characteristics of the photothermal, convection, and phase changes of MPCM. Consequently, the selection of several key MPCM parameters may lack the necessary theoretical support. Without further investigation of the coupling heat transfer mechanisms within the MPCM, optimizing the heat transfer efficacy of RCCS and other MPCM-integrated system may be challenging.

This study developed a computational program to simulate coupled heat transfer processes involving thermal radiation, convection, and phase changes in an MPCM. The effects of light intensity, core–shell ratio, and MPCM diameter on the heat transfer and phase-change processes were systematically analyzed.

2. Model and verification

2.1. Theory model

The heat transfer process involves three major source terms: thermal radiation, latent heat of the phase change core material and heat convection with the surrounding medium, according to Fig. 2. Based on the energy conservation equation [21], the phase-change process of the MPCM can be expressed as

$$\begin{cases} \overline{\rho c}_p \dfrac{dT}{d\tau} = Q_r + Q_h \quad \mathrm{T} \leqslant \mathrm{T}_m \\ \overline{\rho c}_p \dfrac{dT}{d\tau} = Q_r + Q_L + Q_h \quad \mathrm{T} > \mathrm{T}_m \end{cases} \tag{1}$$

where $\overline{\rho}$ is the average density of the MPCM, and $\overline{c}_p$ is the average specific heat. T and τ represent the temperature and time, respectively. T_m is the melting point of the PCM. The heat and cold sources are divided into three parts depending on the heat transfer process, as shown in Fig. 2. The first part Q_r is the heat absorbed by the MPCM from the infrared radiation, and it can be expressed as

$$Q_r = IGQ_{abs} \tag{2}$$

where I is the light intensity, and G is the projected area of the MPCM in the direction of the incident infrared radiation. Q_{abs} is the absorption efficiency, which can be expressed as [22]:

$$Q_{abs} = Q_e - Q_s, \tag{3}$$

$$\begin{aligned} Q_e &= \frac{2}{\chi_2^2}\sum_{n=1}^{\infty}(2n+1)\mathrm{Re}\{a_n + b_n\}, \\ Q_s &= \frac{2}{\chi_2^2}\sum_{n=1}^{\infty}(2n+1)\left[|a_n|^2 + |b_n|^2\right]. \end{aligned} \tag{4}$$

here, Q_e and Q_s are the extinction and scattering efficiencies, respectively. χ_1 and χ_2 are the size parameters of the core and shell of the MPCM, respectively, expressed as

$$\chi_1 = \frac{2\pi R_1}{\lambda}, \tag{5}$$

$$\chi_2 = \frac{2\pi R_2}{\lambda}. \tag{6}$$

here, R_1 and R_2 are the radii of the MPCM core and shell of the MPCM, respectively, and λ is the infrared wavelength. Here, a_n and b_n are expressed as follows [23]:

$$a_n = \frac{\left[\widetilde{D}_n m_0/m_2 + n/(m_0\chi_2)\psi_n(m_0\chi_2)\right] - \psi_{n-1}(m_0\chi_2)}{\left[\widetilde{D}_n m_0/m_2 + n/(m_0\chi_2)\xi_n(m_0\chi_2)\right] - \xi_{n-1}(m_0\chi_2)}, \tag{7}$$

$$b_n = \frac{\left[\widetilde{G}_n m_2/m_0 + n/(m_0\chi_2)\psi_n(m_0\chi_2)\right] - \psi_{n-1}(m_0\chi_2)}{\left[\widetilde{G}_n m_2/m_0 + n/(m_0\chi_2)\xi_n(m_0\chi_2)\right] - \xi_{n-1}(m_0\chi_2)}, \tag{8}$$

$$\widetilde{D}_n = \frac{D_n(m_2\chi_2) - A_n\left[\mathrm{X}_n'(m_2\chi_2)/\psi_n(m_2\chi_2)\right]}{1 - A_n\left[\mathrm{X}_n(m_2\chi_2)/\psi_n(m_2\chi_2)\right]}, \tag{9}$$

$$\widetilde{G}_n = \frac{D_n(m_2\chi_2) - B_n\left[\mathrm{X}_n'(m_2\chi_2)/\psi_n(m_2\chi_2)\right]}{1 - B_n\left[\mathrm{X}_n(m_2\chi_2)/\psi_n(m_2\chi_2)\right]}, \tag{10}$$

$$A_n = \frac{m_2 D_n(m_1\chi_1) - m_1 D_n(m_2\chi_1)}{m_2 D_n(m_1\chi_1)[\mathrm{X}_n(m_2\chi_1)/\psi_n(m_2\chi_1)] - m_1[\mathrm{X}'_n(m_2\chi_1)/\psi_n(m_2\chi_1)]}, \tag{11}$$

$$B_n = \frac{m_1 D_n(m_1\chi_1) - m_2 D_n(m_2\chi_1)}{m_1 D_n(m_1\chi_1)[\mathrm{X}_n(m_2\chi_1)/\psi_n(m_2\chi_1)] - m_2[\mathrm{X}'_n(m_2\chi_1)/\psi_n(m_2\chi_1)]}, \tag{12}$$

where φ_n, X_n, and ξ_n are the *Ricatti–Bessel functions* associated with the *Spherical Bessel function* of the first kind j_n, the *Spherical Bessel function* of the second kind y_n, and the *Hankel function* $h_n^{(1)}$, respectively. The parameters m_0, m_1, and m_2 are the complex refractive indices of the host fluid [24], core, and shell, respectively. D_n is the logarithmic derivative of φ_n.

$$D_n = \frac{\varphi'_n}{\varphi_n} \tag{13}$$

The second part of the left-hand side of the energy conservation equation is Q_h, which is the heat exchanged between the MPCM and external fluid.

$$Q_h = h(T - T_L)S \tag{14}$$

here, T_L is the temperature of the host fluid, and S is the surface area of the MPCM, given as $4\pi R_2^2$. The h is the convective heat transfer coefficient derived from *Nu*.

$$Nu = \frac{2hR_2}{k_2} \tag{15}$$

where k_2 is the thermal conductivity of the shell.

Here in, the Nusselt number of the sphere in water flow was calculated via ANSYS Fluent. The k-ε turbulence model and the SIMPLE method is adopted. The convergence criteria set at residuals below 1e-5 for all equations except the energy conservation (less than 1e-8). Grid independence was validated as shown in Fig. 3, confirming Nu deviations below 3.7 % between models with 200,000 and 3,850,000 grids. Hence, 200,000 grids were selected for the simulation.

As shown in Fig. 4, the results of the original empirical relationship (green line) are not consistent with that of the Fluent simulation at the micrometer scale. More importantly, the difference between the two results increases significantly with an increase in *Re*. Thus, a new correction needs to be proposed. Zhang et al. [25] used the formulation of this structure in their fitting of *Sh*:

Fig. 3. Grid sensitivity validation of Fluent simulation.

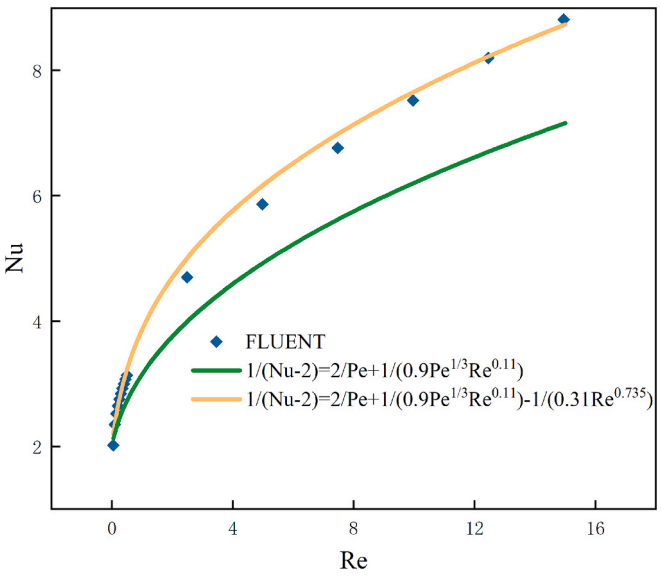

Fig. 4. Comparison of the Fluent simulation results and empirical calculation formulas.

$$\frac{1}{(Sh-2)^n} = \frac{1}{(0.5Pe + 0.3026Pe^2)^n} + \frac{1}{(1.008Pe^{1/3})^n} \tag{16}$$

The formula fits the experimental data well when n = 3. Finlayson et al. [26] were inspired to propose the formula in their fit to *Nu*:

$$\frac{1}{(Nu-2)^n} = \frac{1}{(Pe/2)^n} + \frac{1}{(cPe^{1/3}Re^m)^n} \tag{17}$$

where *Re* is added to the denominator of the second term on the right side of the equation to enhance the effect of *Re* on *Nu*, the equation fits better at $Re < 1$ when n = 1, c = 0.9 and m = 0.11. However, significant deviations from calculated values arise at $Re > 10$. To further enhance the positive effect of *Re* on *Nu* in the above framework, a separate term relating only to *Re* is added to the right-hand side of the formula and the term is negative. The resulting equation is as follows:

$$\frac{1}{(Nu-2)^n} = \left(\frac{2}{Pe}\right)^n + \left(\frac{1}{c_1 Pe^{1/3}\mathrm{Re}^m}\right)^n - \left(\frac{1}{c_2 \mathrm{Re}^k}\right)^n \tag{18}$$

The third part is Q_L, which is the heat absorbed by the phase transition [27].

$$Q_L = \frac{k_l(T - T_m)V_c}{R_1^2 \rho_l} \frac{3(1-f_l)^{\frac{1}{3}}}{[k_l/(hR_2) - 1](1-f_l)^{\frac{1}{3}} + 1} \tag{19}$$

where k_l and ρ_l are the thermal conductivity and density of the liquid-phase material, respectively, f_l is the liquid volume of the core, and V_c is the core volume of the MPCM.

2.2. Program verification

A transient calculation program for the radiative heat transfer of a single MPCM was developed using Python [28]. The accuracy of the program was verified by comparison with the simulation results of a COMSOL Ray Optic Module. The light-intensity distribution of diffraction is as follows [29]:

$$I(P) = I_0 \frac{4\pi^2 r^4}{f^2 \lambda^2} \left[\frac{2J_1(kr\sin\theta)}{kr\sin\theta}\right]^2 \tag{20}$$

where P refers to a point in the focal plane; I_0 and λ are the intensity and wavelength of the incident planar light, respectively; f is the focal

length; r is the radius of the MPCM; and k is the wave number.

Fig. 5 shows the light intensity distribution of diffraction for $\lambda = 0.8$ μm and $R_1 = 25$ μm, indicating that a considerable amount of the diffracted light is in the same direction as the incident light. Therefore, diffraction is not considered under this condition [30].

Table 1 presents the parameters of grid sensitivity verification, including geometric and ray grids. The temperature-dependent complex refractive indices of the shell (TiO_2) [31] and core materials (paraffin) [32] were set. As shown in Fig. 6, results reveal that the deviation between the final steady-state average temperature of models with more than 100,000 geometric and 40,000 ray grids is less than 0.1 %. Hence, 200,000 geometric and 62,500 ray grids were sufficient to guarantee accuracy and were selected for the simulation.

Fig. 7 shows the final steady-state average temperature of the COMSOL simulation and Python calculation. The calculated results are consistent with the simulation results. Although the calculated results are slightly higher than the simulation results, the maximum deviation is less than 0.8 %.

3. Results and discussion

Based on the MPCM phase-change-process calculation program, the fundamental characteristics of the heat transfer environment and MPCM can be further analyzed. This section evaluates the influence of thermal radiation intensity, MPCM core–shell ratio, and particle diameter on heat transfer performance. Except these three parameters discussed in the subsections, the setting of the remaining key parameters is based on Table 1. Additionally, the relationship between the phase-change process and MPCM diameter is elucidated, revealing two critical diameters that significantly affect the phase-change process. Furthermore, the dependence of these critical diameters on thermal radiation intensity is established.

3.1. Effect of light absorption on phase-change process

As can be seen from the Fig. 8 and Fig. 9, the difference between the temperature rise curve and the phase change curve is extremely small at constant optical parameters and temperature dependent optical parameters. This is due to the fact that the optical absorption coefficient Q_{abs} of the MPCM grows from 0.80924 to 0.81168 only by 0.302 % in the temperature range shown in the figure. Therefore, although the component materials of the MPCM have a change in the complex refractive index due to temperature and phase change, this change is negligible for the heat transfer and phase change process of this type of MPCM under the normal conditions of application.

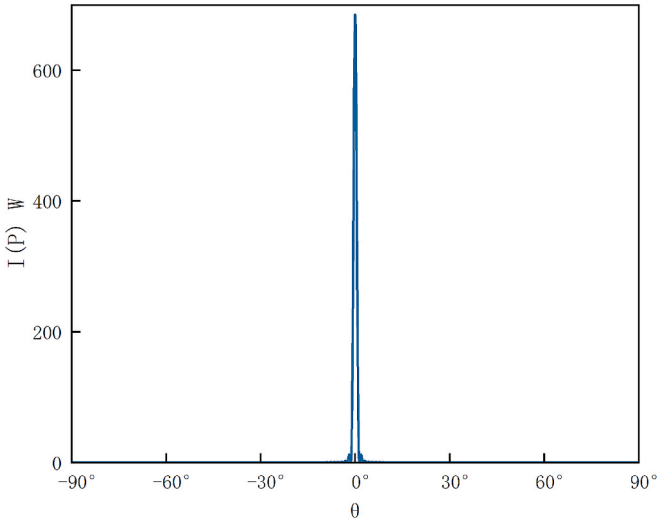

Fig. 5. Light intensity distribution of diffraction.

Table 1
Parameters of the grid sensitivity verification.

Parameter	Value
Diameter (μm)	50
Core-shell ratio	0.5
Wavelength (μm)	0.8
Light intensity (W/m^2)	4×10^6
Phase change temperature (K)	313.15
Liquid temperature (K)	300

Fig. 10 shows a comparison of the variations in temperature vs. time under different light intensities. The final steady-state temperature increases gradually with increasing light intensity. The time required to reach the final steady state decreases with increasing light intensity, except for an intensity of 1×10^6 W/m^2. The reason for the exception is illustrated in Fig. 11, indicating that phase-change do not occur at this light intensity. As shown in Fig. 11, the main cause of the reduction in time is the acceleration of the phase change with increasing light intensity. If Q_r and Q_L are considered as terms that do not vary with temperature, combined with the boundary condition $T(0) = T_L$, solving Eq. (1) can be obtained:

$$\begin{cases} T(\tau) = T_L + \dfrac{Q_r}{hS}\left(1 - e^{-\frac{\tau}{\tau_c}}\right) & T \leqslant T_m \\ T(\tau) = T_L + \dfrac{Q_r + Q_L}{hS}\left(1 - e^{-\frac{\tau}{\tau_c}}\right) & T > T_m \end{cases} \tag{21}$$

where τ_c is:

$$\tau_c = \frac{\overline{\rho c}_p V}{hS} \tag{22}$$

When the light intensity is 1×10^6 W/m^2, making Q_r too small, hence:

$$T(\infty) = T_L + \frac{Q_r}{hS} < T_m \tag{23}$$

Eventually, the phase change cannot occur. When the light intensity is 3×10^6 W/m^2, the absolute value of Q_r and Q_L (Q_L is negative) in the phase change stage is close to each other, resulting in the decrease of the slope of the temperature rise curve. When the light intensity is stronger, the phase change stage Q_r is obviously larger than Q_L, and the phase change has a limited effect on the coefficient of the exponent in the above equation, which makes the temperature basically grow according to the exponential law in the above equation with time.

3.2. Effect of core-shell ratio on phase-change process

Fig. 12 and Fig. 13 illustrate the effect of core–shell ratio on the variations in temperature and phase change, respectively. As shown in Fig. 12, the final steady-state temperature is almost unaffected by the core–shell ratio. The temperature slightly decreases only when the core–shell ratio reaches 0.9. This result indicates that coating the surface of the MPCM can substantially affect its photothermal conversion properties, even when the coating is extremely thin. In particular, when the core–shell ratio is 0, the system represents a particle composed solely of the MPCM shell material. For core–shell ratios below 0.3, the temperature rise profile of the MPCM closely mirrors that of particles containing no phase-change material. This suggests that the phase change of the core material has negligible impact on the MPCM's thermal behavior when the core volume is small. As the core–shell ratio increases, two key trends emerge: (1) the slope of the temperature rise curves decreases during the MPCM phase change stage, and (2) the time required for the MPCM to reach thermal equilibrium increases progressively. These observations further indicate that, for a fixed MPCM size, the core volume has minimal influence on the material's light absorption capacity.

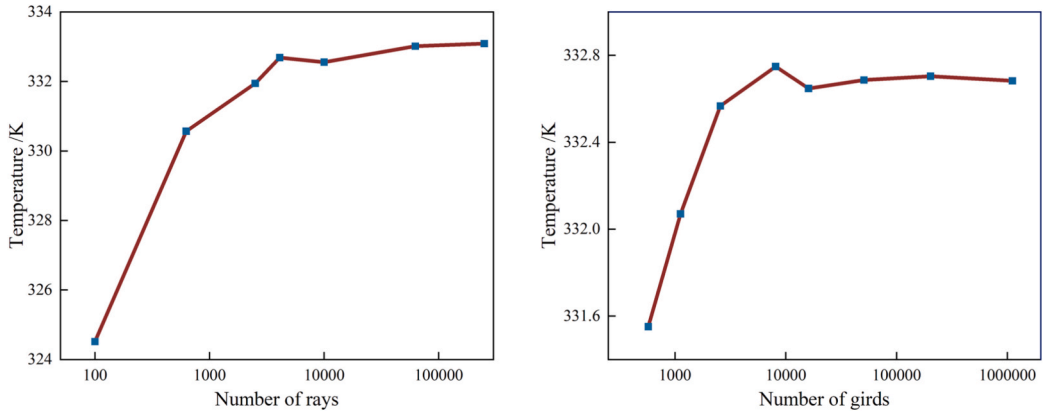

Fig. 6. Grid sensitivity validation of COMSOL simulation.

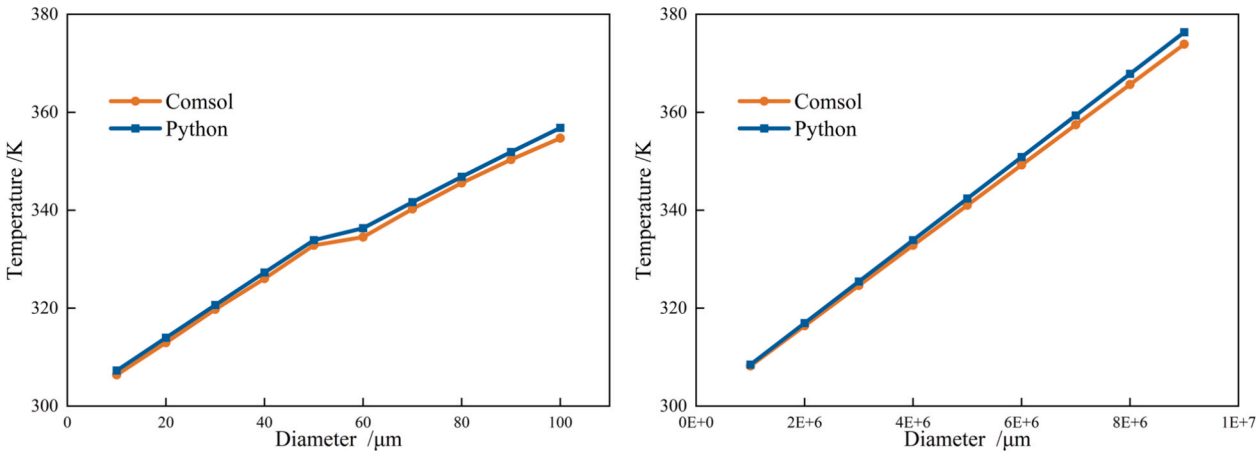

Fig. 7. Comparison between COMSOL simulation and Python calculation results.

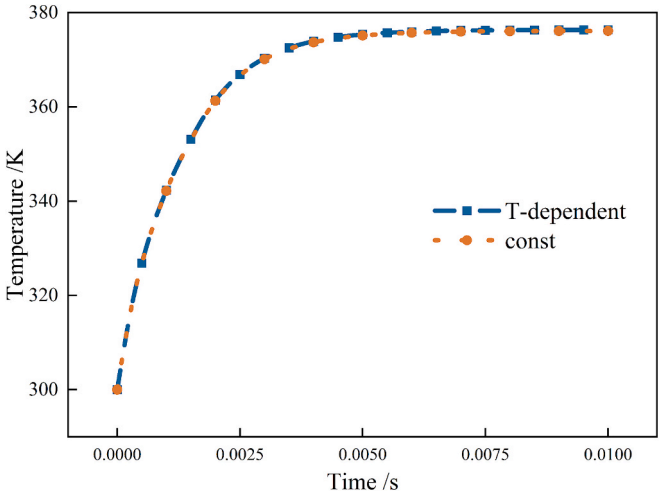

Fig. 8. Effect of optical parameter on temperature.

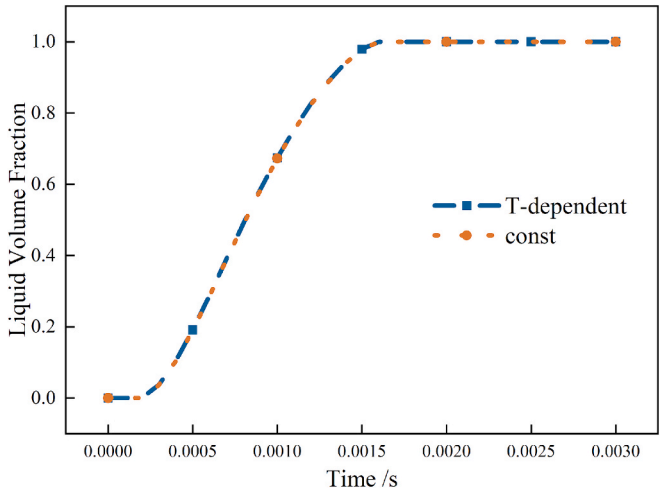

Fig. 9. Effect of optical parameter on phase change.

Fig. 13 shows that the phase-change time increases exponentially as the core–shell ratio increases.

3.3. Effect of MPCM diameter on phase-change process

Fig. 14 and Fig. 15 show the results of temperature variation and phase-change, combining data for MPCM diameters ranging from 10 to 90 μm. In this case, the light intensity is set to 4×10^6 W/m^2, and the core–shell ratio is 0.5.

As shown in Fig. 14, the final steady-state temperature rises as the diameter increases. This discrepancy can be attributed to the reduction in the Nusselt number. Based on the revised empirical relation, the Nusselt number of MPCM is inversely proportional to the particle size.

Therefore, phase-change does not occur when the diameter is 10 μm,

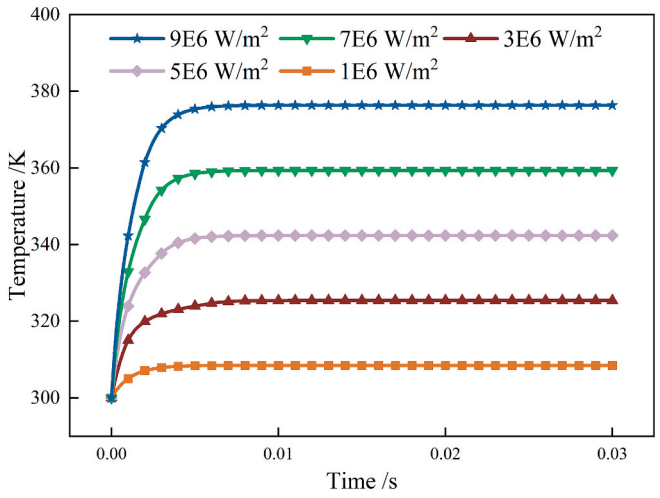

Fig. 10. Effect of light intensity on temperature.

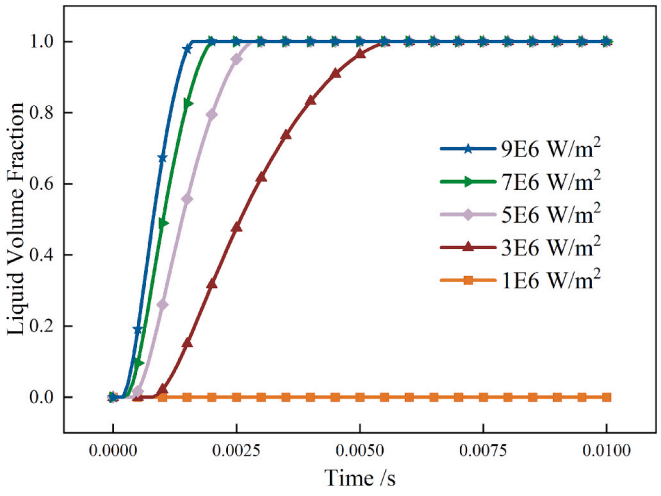

Fig. 11. Effect of light intensity on phase change.

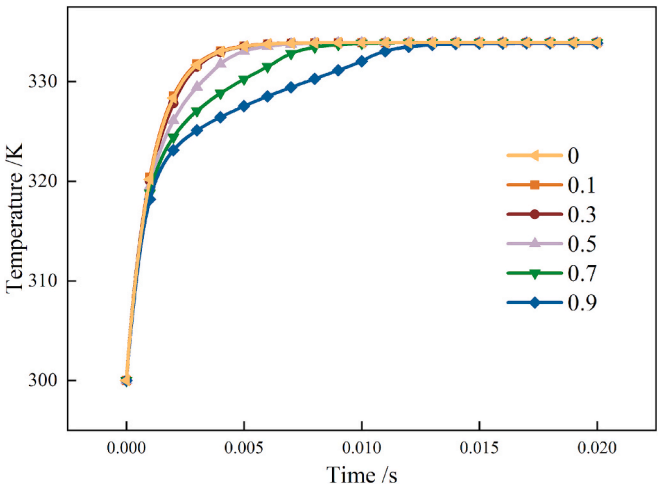

Fig. 12. Effect of core–shell ratio variations on temperature.

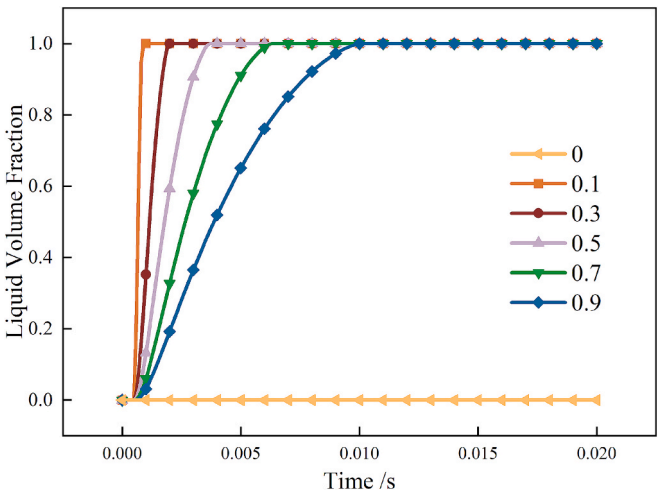

Fig. 13. Effect of core–shell ratio on phase change.

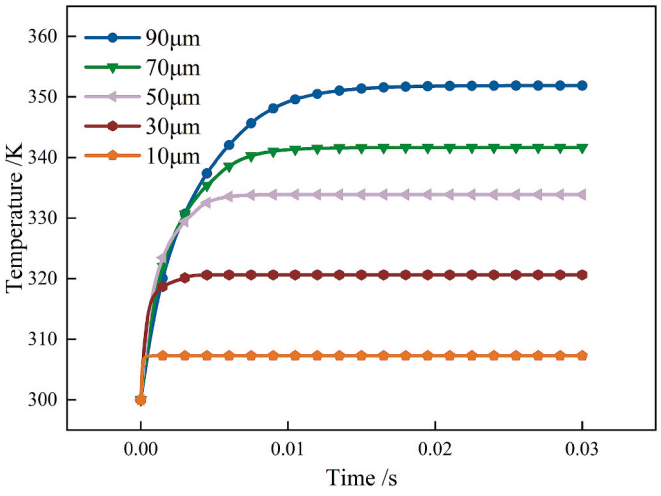

Fig. 14. Effect of diameter variations on temperature (from 10 to 90 μm).

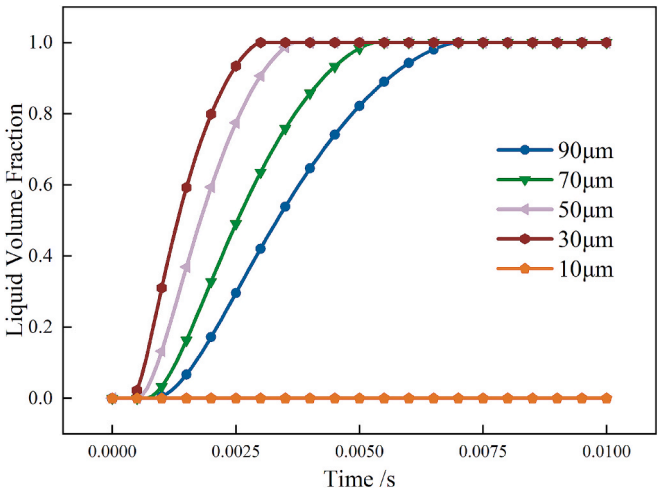

Fig. 15. Effect of diameter on phase change (from 10 to 90 μm).

as shown in Fig. 15. Fig. 16 shows the same type of data as those in Fig, 6 but for a diameter range of 15 to 35 μm. Herein, the most noticeable result is that the phase-change time is significantly longer for an MPCM with a 20-μm diameter than for MPCMs with different diameters.

Furthermore, Fig. 17 shows the phase-change times of MPCMs of various diameters. The asymptotic line, which is the dividing line

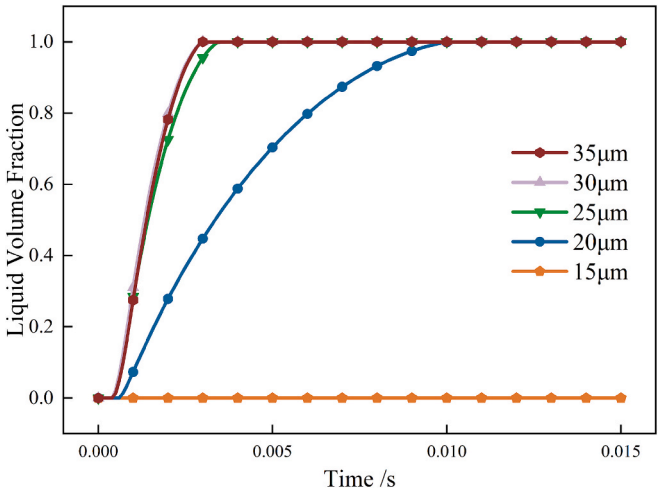

Fig. 16. Effect of diameter on phase change (from 15 to 35 μm).

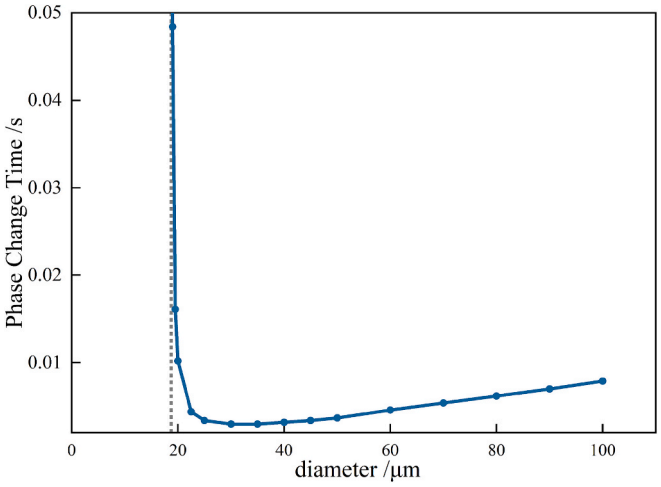

Fig. 17. Phase change time of different MPCM diameters.

indicating the occurrence of a phase-change, is noticeable in the figure. The x-coordinate of this line depends on the final steady-state temperature, which is equal to the phase-change temperature. From eq. (1), the relational equation can be expressed as

$$\frac{\mathrm{IQ}_{abs}(\overline{m},\overline{r})}{4} = h(r_s,p,u)\times(T_m - T_L) \tag{24}$$

where $\overline{m}$ is the combination of m_s, m_c, and m_l; $\overline{r}$ is the combination of r_s and r_c; p represents the properties of the base fluid. Considering the oscillation of Q_{abs} with $\overline{r}$.

The critical diameter (d_{cr}) calculation program was developed using dichotomy. As shown in Fig. 17, the result in this condition is 18.56 μm. Another critical observation in Fig. 17 is the minimum phase-change time, appearing in the range of 30 to 35 μm. For convenience, the diameter corresponding to the minimum phase-change time is denoted as the most effective diameter (d_e). The parameter d_e may be influenced by the following: 1) the convective heat transfer coefficient (h), which decreases exponentially as d increases; 2) the volume of the phase-change material, which is proportional to the cube of d; consequently, the amount of heat required for a complete phase change increases with d; and 3) Q_{abs}, which increases with d, but its rate of change is significantly smaller than those of the other two factors. In conclusion, when d approaches the critical value (d_{cr}), h increases significantly and consequently, the net heat flow into the MPCM reduces considerably, resulting in a substantially longer phase-change time. As d_{cr} increases to d_e, the net heat flow sharply increases following a decrease in h. Hence, the phase-change time is reduced to a minimum. As d increases continuously, the effect of h on the phase change is no longer dominant. Rather, the increase in the volume of the phase-change material results in a steady-state increase in time. This finding may offer a new explanation for the observed phenomenon in Fig. 18 of Ref. [10], where the heat capacity of MPCM slurry shows negligible improvement when the particle size is reduced below 50 μm.

A further analysis of d_{cr} and d_e is illustrated in Fig. 18, indicating that d_{rc} and d_e decrease as the light intensity increases. In addition, the decrease in d_{rc} and d_e becomes increasingly smaller with an increase in light intensity. In particular, as the light intensity increases, the phase change time and radius change trend become increasingly closer.

Fig. 19 and Fig. 20 show the variations in d_{cr} and d_e with light intensity, respectively. The calculation results of the program are indicated by blue dots. The fitting functions are represented by orange curves. The correlation formula are as follow:

$$\begin{aligned} d_{cr} &= 7.290\times10^{8} I^{-1.15} \\ d_e &= 1.118\times10^{9} I^{-1.14} \end{aligned} \tag{25}$$

The R^2 values of the two formulas are 0.99846 and 0.99752, respectively. The expressions of the fitting functions indicate that d_{cr} and d_e are inversely proportional to I. This relation can be attributed to the empirical correlation of h. In Fig. 20, the light-blue zone indicates the variable range of d_e, within which the difference in the phase-change time is less than 0.0001. The discrepancy in the zone size can probably be attributed to the oscillation of Q_{abs} with d. Therefore, further refinement of the algorithm is necessary to eliminate the effects of oscillation and accurately determine d_e. It is important to note that the heat transfer environment in practical applications is significantly more complex than the conditions assumed in the calculations. For instance, light intensity varies over time, and the temperature of the host medium changes noticeably as the volume fraction of the MPCM increases. Consequently, applying the above model to the study of MPCM flow and heat transfer remains a considerable challenge. Additionally, the findings require more detailed discussion and validation in real-world scenarios.

4. Conclusion

This study investigates the coupled heat transfer mechanism of the MPCM in a environment involving both convection and thermal radiation. A computational program was developed to analyze the heat transfer characteristics of the MPCM, providing an effective tool for

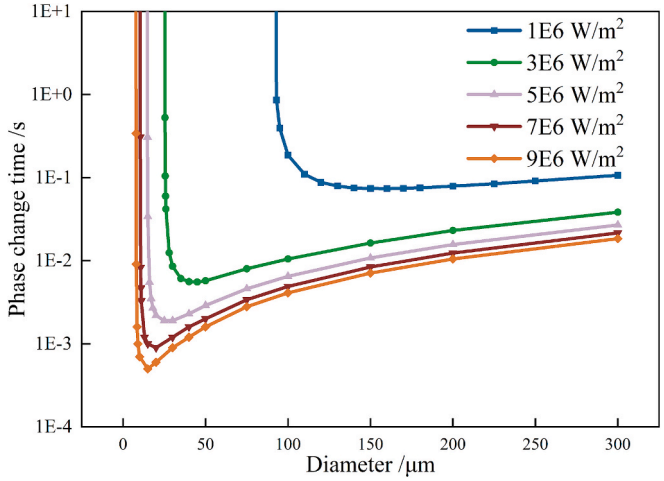

Fig. 18. Phase change time of MPCM under different light intensities.

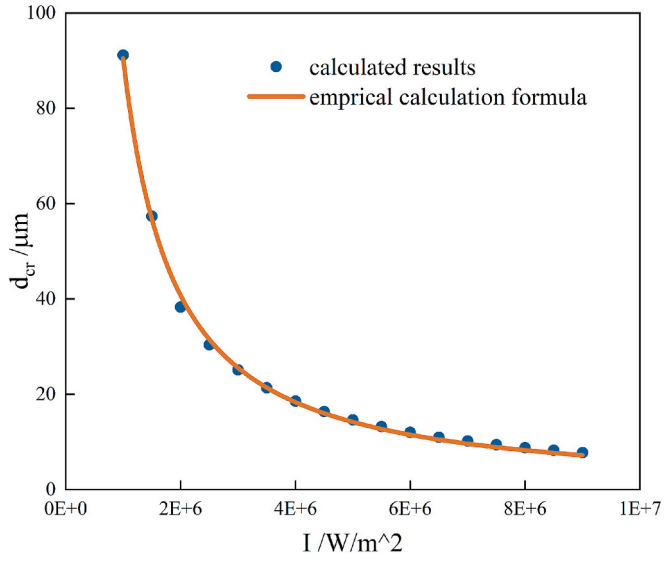

Fig. 19. d_{cr} under different light intensities.

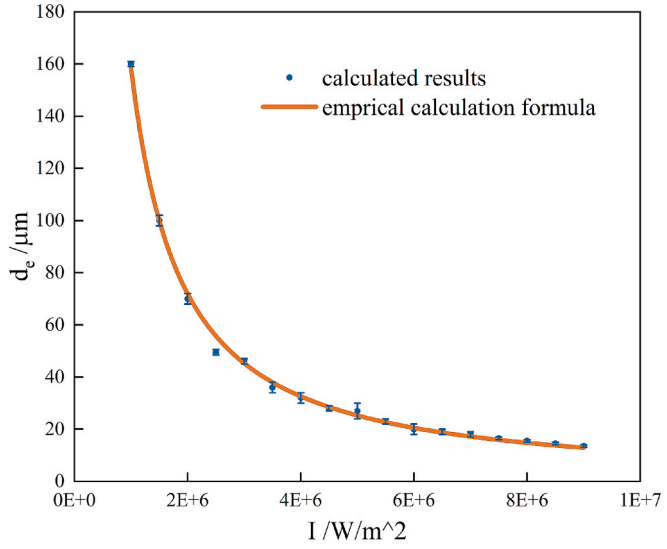

Fig. 20. d_e under different light intensities.

detailed investigation and optimization. The effects of light intensity, core–shell ratio, and MPCM diameter on heat transfer and phase change processes were systematically analyzed. The analysis would offer valuable guidance for selecting an appropriate particle size range in practical applications. The main conclusions are obtained as follows:

1. A computational program was developed to simulate the transient coupled heat transfer of MPCM. The reliability of the program was validated by comparing its results with simulation results obtained using the commercial multiphysics simulation software. The maximum deviation between them is less than 0.8 %.
2. As the light intensity increased, the final steady-state temperature of the MPCM increased steadily, whereas the phase-change time decreased sharply. The final steady-state temperature remained unaffected by variations in the core–shell ratio. However, the phase-change time increased exponentially with an increase in the core–-shell ratio.
3. The critical diameter d_{cr} and most effective diameter d_e were proposed. The critical diameter determines whether a phase change in the MPCM occurs, and the most effective diameter has the shortest phase-change time.
4. The variations in the d_{cr} and the d_e with light intensity were analyzed and summarized. Computational programs were developed to calculate these diameters, and two empirical correlation formulas were proposed. These formulas demonstrated strong agreement with the calculated results, validating their accuracy and applicability.

CRediT authorship contribution statement

Si Yang: Writing – original draft, Validation, Software, Methodology, Investigation, Formal analysis, Data curation. **Hangbin Zhao:** Writing – review & editing, Supervision, Project administration, Conceptualization. **Renwei Tang:** Methodology, Formal analysis. **Xiaobin Tang:** Writing – review & editing, Supervision, Conceptualization.

Declaration of competing interest

The authors declare that they have no known competing financial interests or personal relationships that could have appeared to influence the work reported in this paper.

Acknowledgements

This research is jointly supported by the National Natural Science Foundation of China (Grant No. 12205152), the Natural Science Foundation of Jiangsu Province (Grant No. BK20220904) and the Graduate Research Innovation Program Project of Jiangsu Province (Grant No. KYCX25_0610).

Data availability

Data will be made available on request.

References

[1] R. Freile, M. Tano, P. Balestra, S. Schunert, M. Kimber, Improved natural convection heat transfer correlations for reactor cavity cooling systems of high-temperature gas-cooled reactors: from computational fluid dynamics to Pronghorn, Ann. Nucl. Energy 163 (2021).
[2] H. Qin, X. Li, X. Liu, L. Zhang, X. Wu, Y. Zheng, Heat removal power analysis of HTR-PM passive reactor cavity cooling system, Yuanzineng Kexue Jishu 57 (2023) 225–233.
[3] H.S. Lim, N.-I. Tak, S.N. Lee, C.K. Jo, Water-jacket reactor cavity cooling system concept to mitigate severe accident consequence of high temperature gas-cooled reactor, Nucl. Eng. Des. 340 (2018) 156–165.
[4] J. Tong, D. Wang, Z. Wu, Z. Zhang, Development strategy of high temperature gas cooled reactor in China, Chin. J. Eng. Sci. 21 (2019).
[5] K. Qin, N. Zhuang, C. Shao, H. Zhao, X. Tang, Gyroid-type TPMS structure optimization based on mathematical function control and its convective heat transfer performance study, Int. Commun. Heat Mass Transf. 162 (2025) 108682.
[6] M.A. Al-Obaidi, F.L. Rashid, M.K. Rasheed, H.S.S. Aljibori, H.I. Mohammed, A. J. Mahdi, S. Ahmad, K. Al-Farhany, I.M. Mujtaba, Recent achievements in heat transfer enhancement with hybrid nanofluid in heat exchangers: a comprehensive review, Int. J. Thermophys. 45 (2024) 133.
[7] Q. Xu, L. Zhu, Y. Pei, C. Yang, D. Yang, Z. Liu, B. Guan, Y. Qiang, H. Yang, Y. Zang, Y. Ding, Heat transfer enhancement performance of microencapsulated phase change materials latent functional thermal fluid in solid/liquid phase transition regions, Int. J. Heat Mass Transf. 214 (2023) 124461.
[8] R. Zeng, X. Wang, B. Chen, Y. Zhang, J. Niu, X. Wang, H. Di, Heat transfer characteristics of microencapsulated phase change material slurry in laminar flow under constant heat flux, Appl. Energy 86 (2009) 2661–2670.
[9] M.S. Ghoghaei, A. Mahmoudian, O. Mohammadi, M.B. Shafii, H. Jafari Mosleh, M. Zandieh, M.H. Ahmadi, A review on the applications of micro-/nano-encapsulated phase change material slurry in heat transfer and thermal storage systems, J. Therm. Anal. Calorim. 145 (2021) 245–268.
[10] R. Sabbah, J. Seyed-Yagoobi, S. Al-Hallaj, Heat transfer characteristics of liquid flow with micro-encapsulated phase change material: numerical study, J. Heat Transfer 133 (2011).
[11] A. Lenert, Y. Nam, B.S. Yilbas, E.N. Wang, Focusing of phase change microparticles for local heat transfer enhancement in laminar flows, Int. J. Heat Mass Transf. 56 (2013) 380–389.

[12] Q. Lin, S. Wang, L. Zhang, Multi-scale modeling and investigation of thermo-fluidic performance of microencapsulated phase-change material slurry, J. Storage Mater. 37 (2021).
[13] H. Zhao, R. Tang, N. Zhuang, X. Tang, Numerical study on the thermal performance of space radiator using microencapsulated phase change material slurry as working medium, Appl. Therm. Eng. 258 (2025) 124700.
[14] W. Su, Y. Li, T. Zhou, J. Darkwa, G. Kokogiannakis, L. Zhao, Microencapsulation of paraffin with poly (urea methacrylate) shell for solar water heater, Energies 12 (2019).
[15] Y.-K. Kang, J. Joung, M. Kim, J.-W. Jeong, Energy impact of heat pipe-assisted microencapsulated phase change material heat sink for photovoltaic and thermoelectric generator hybrid panel, Renew. Energy 207 (2023) 298–308.
[16] F. Ma, P. Zhang, Performance investigation of the direct absorption solar collector based on phase change slurry, Appl. Therm. Eng. 162 (2019) 114244.
[17] F. Ran, H. Zhang, C. Xu, G. Fang, Thermal performances evaluation of a flat-plate solar collector using microencapsulated phase-change slurry as heat transfer medium, Int. J. Energy Res. 46 (2022) 14044–14059.
[18] M. Karami, N. Shahini, M. Ali Akhavan Behabadi, Numerical investigation of double-walled direct absorption evacuated tube solar collector using microencapsulated PCM and nanofluid, J. Mol. Liq. 377 (2023).
[19] Z. Wang, J. Qu, R. Zhang, X. Han, J. Wu, Photo-thermal performance evaluation on MWCNTs-dispersed microencapsulated PCM slurries for direct absorption solar collectors, J. Storage Mater. 26 (2019) 100793.
[20] H. Huang, T. Shi, R. He, J. Wang, P.K. Chu, X.F. Yu, Phase-changing microcapsules incorporated with black phosphorus for efficient solar energy storage, Adv. Sci. 7 (2020).
[21] T.L. Bergman, Fundamentals of Heat and Mass Transfer, John Wiley & Sons, 2011.
[22] C.F. Bohren, D.R. Huffman, Absorption and Scattering of Light by Small Particles, John Wiley & Sons, 2008.
[23] P. Yang, B.-C. Gao, W.J. Wiscombe, M.I. Mishchenko, S.E. Platnick, H.-L. Huang, B. A. Baum, Y.X. Hu, D.M. Winker, S.-C. Tsay, Inherent and apparent scattering properties of coated or uncoated spheres embedded in an absorbing host medium, Appl. Opt. 41 (2002) 2740–2759.
[24] G.M. Hale, M.R. Querry, Optical constants of water in the 200-nm to 200-μm wavelength region, Appl. Opt. 12 (1973) 555–563.
[25] S.H. Zhang, E.J. Davis, Masstransfer from a single micro-droplet to a gas flowing at low reynolds number, Chem. Eng. Commun. 50 (1987) 51–67.
[26] B.A. Finlayson, J.W. Olson, Heat transfer to spheres at low to intermediate Reynolds numbers, Chem. Eng. Commun. 58 (1987) 431–447.
[27] L.C. Tao, Generalized numerical solutions of freezing a saturated liquid in cylinders and spheres, AIChE J. 13 (1967) 165–169.
[28] B.J. Sumlin, W.R. Heinson, R.K. Chakrabarty, Retrieving the aerosol complex refractive index using PyMieScatt: a Mie computational package with visualization capabilities, J. Quant. Spectrosc. Radiat. Transf. 205 (2018) 127–134.
[29] G.B. de Boer, C. de Weerd, D. Thoenes, H.W. Goossens, Laser diffraction spectrometry: Fraunhofer diffraction versus Mie scattering, Part. Part. Syst. Charact. 4 (1987) 14–19.
[30] M.Q. Brewster, Thermal Radiative Transfer and Properties, John Wiley & Sons, 1992.
[31] Y.-N. Wu, W.A. Saidi, P. Ohodnicki, B. Chorpening, Y. Duan, First-principles investigations of the temperature dependence of electronic structure and optical properties of rutile TiO_2, J. Phys. Chem. C 122 (2018) 22642–22649.
[32] D. Zhao, G. Zhang, X. Zhang, D. Li, Optical properties of paraffin at temperature range from 40 to 80 °C, Optik 157 (2018) 184–189.